Control of instability by injection rate oscillations in a radial Hele-Shaw cell

Rahul Arun [1,*] Scott T. M. Dawson [2] Peter J. Schmid [3]
Angeliki Laskari [4] and Beverley J. McKeon [1]

[1]*Graduate Aerospace Laboratories, California Institute of Technology, Pasadena, California 91125, USA*
[2]*Department of Mechanical, Materials, and Aerospace Engineering, Illinois Institute of Technology, Chicago, Illinois 60616, USA*
[3]*Department of Mathematics, Imperial College London, London SW7 2AZ, United Kingdom*
[4]*Department of Process and Energy, Delft University of Technology, 2600 AA Delft, Netherlands*

(Received 6 May 2020; accepted 28 November 2020; published 17 December 2020)

Small spatial perturbations grow into fingers along the unstable interface of a fluid displacing a more viscous fluid in a porous medium or a Hele-Shaw cell. Mitigating this Saffman-Taylor instability increases the efficiency of fluid displacement applications (e.g., oil recovery), whereas amplifying these perturbations is desirable in, e.g., mixing applications. In this work, we investigate the Saffman-Taylor instability through analysis and experiments in which air injected with an oscillatory flow rate outwardly displaces silicone oil in a radial Hele-Shaw cell. A solution for linear instability growth that shows the competing effects of radial growth and surface tension, including wetting effects, is defined given an arbitrary reference condition. We use this solution to define a condition for stability relative to the constant flow rate case and make initial numerical predictions of instability growth by wave number for a variety of oscillations. These solutions are then modified by incorporating reference conditions from experimental data. The morphological evolution of the interface is tracked as the air bubble expands and displaces oil between the plates. Using the resulting images, we analyze and compare the linear growth of perturbations about the mean interfacial radius for constant injection rates with and without superimposed oscillations. Three distinct types of flow rate oscillations are found to modulate experimental linear growth over a constant phase-averaged rate of fluid displacement. In particular, instability growth at the interface is mildly mitigated by adding to the base flow rate provided by a peristaltic pump a second flow with low-frequency oscillations of small magnitude and, to a lesser extent, high-frequency oscillations of large amplitude. In both cases, the increased stability results from the selective suppression of the growth of large wave numbers in the linear regime. Contrarily, intermediate oscillations consistently destabilize the interface and significantly amplify the growth of the most unstable wave numbers of the constant flow rate case. Numerical predictions of low-frequency oscillations of opposite sign (initially decreasing) show promise of even greater mitigation of linear instability growth than that observed in this investigation. Looking forward, proper characterization of the unsteady, wetting, and nonlinear dynamics of instability growth will give further insight into the efficacy of oscillatory injection rates.

DOI: 10.1103/PhysRevFluids.5.123902

I. INTRODUCTION

When one fluid displaces another of larger viscosity in a porous medium, small wavelike perturbations at the fluid-fluid interface grow and resemble "fingers" in a process known as viscous

*rarun@caltech.edu

 ©2020 American Physical Society

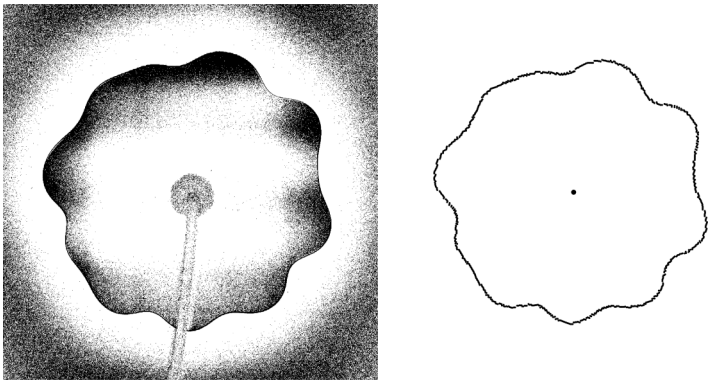


FIG. 1. Experimentally obtained, background-subtracted photograph (left) showing the Saffman-Taylor instability along the interface between air outwardly displacing silicone oil. The interface represented as a discretized boundary (right) that is uniformly partitioned by angle, as produced by the methods discussed in Sec. III.

fingering, or the Saffman-Taylor instability. The ability to prescribe flow conditions that amplify or attenuate this instability is desirable in a variety of engineering applications, such as petroleum engineering. For example, when water jets displace oil reservoirs in porous rocks, widespread fingering reduces secondary oil-recovery yield, which often hinders the extraction of the majority of oil in the reservoir [1]. Further, numerical simulations suggest that cyclically water-flooding oil reservoirs can significantly improve the overall yield [2]. Another study showed that withholding injection for a significant duration can retract fingers after an initial injection period [3]. As such, unobtrusively mitigating viscous fingering directly benefits many fluid applications and, further, time-varying control schemes show promise in achieving this goal. However, numerous benefits derive from instability amplification as well. For example, amplifying instabilities can increase mixing efficiency in microfluidic applications [4]. Additionally, a recent model suggests that the structural integrity of hydraulic fractures can be improved when displacing the slurry used to hold the fracture open by allowing viscous fingering to dominate over density-based gravitational effects [5]. Further, viscous fingering affects the efficiency of CO_2 sequestration in terms of the pore-space utilized for long-term CO_2 storage in, e.g., saline aquifers [6]. Improving the efficiency of these and other engineering processes motivates the present investigation, in which we aim to theoretically and experimentally control (i.e., amplify or attenuate) the Saffman-Taylor instability.

When the flow is governed by Darcy's law (e.g., in a porous medium), the interface between two immiscible fluids becomes unstable if the displaced fluid has a higher viscosity than the displacing fluid [7]. Flow between two closely spaced parallel plates (i.e., in a Hele-Shaw cell) is analogous to flow in a porous medium since it is also governed by Darcy's law. An example of the Saffman-Taylor instability during outward flow in the radial Hele-Shaw cell configuration is shown in Fig. 1.

The continuous interface is defined in terms of its radius $r(\theta, t)$ from the point of injection for all angular coordinates θ at any time t during injection, assuming $r(\theta, t)$ is not multivalued. A small, spatial perturbation of the interface about its mean, $R(t)$, is defined as $a(\theta, t) = r(\theta, t) - R(t)$. Since the Fourier modes form a complete basis of the angular domain, the perturbation can be decomposed into an infinite sum of wavelike functions as

$$a(\theta, t) = \sum_{n=1}^{\infty} A_n f_n(t) e^{in\theta}, \tag{1}$$

where $n = 1, 2, 3, \ldots$ and the $n = 0$ term can be excluded by assuming a zero-mean perturbation. The behavior of $f_n(t)$ governs the instability dynamics in the linear regime. The spatial parameter

A_n scales instability growth for each wave number, and can be expressed independently of wave number by imposing appropriate reference conditions on $f_n(t)$.

The analysis of [8] considered specifically the case of incompressible flow, driven by a constant flow rate (CFR), in a radial Hele-Shaw cell with constant spacing b between the parallel plates. In this case, the area flow rate Q is defined as the time rate of change of the area enclosed by the bubble from the viewpoint of Fig. 1. Consequently, the mean interfacial radius is given by

$$R(t) = \left[R(0)^2 + \frac{Qt}{\pi}\right]^{\frac{1}{2}}, \tag{2}$$

where Q is the area flow rate, i.e., Qb is the volume flow rate, and the initial bubble radius $R(0)$ is given at $t = 0$. Neglecting wetting effects, the linear instability growth rate for the CFR case is defined as

$$\frac{f_n'(t)}{f_n(t)} = \frac{n-1}{R(t)^2}\left(\frac{Q}{2\pi} - \frac{n(n+1)\sigma M_2}{R(t)}\right), \tag{3}$$

where σ is the surface tension and μ_2 and $M_2 = \frac{b^2}{12\mu_2}$ are the viscosity and mobility of the displaced fluid, respectively. As in [8], the critical (largest) wave number n_c predicted to grow and the maximally growing wave number n_m are determined by solving $f_n'(t) = 0$ and $\frac{\partial}{\partial n}[f_n'(t)] = 0$, respectively. The expressions for the time evolution of these wave numbers are given by

$$n_c(t) = \left(\frac{QR(t)}{2\pi\sigma M_2} + \frac{1}{4}\right)^{\frac{1}{2}} - \frac{1}{2}, \tag{4a}$$

$$n_m(t) = \left[\frac{1}{3}\left(\frac{QR(t)}{2\pi\sigma M_2} + 1\right)\right]^{\frac{1}{2}}. \tag{4b}$$

Half a century after Saffman and Taylor's namesake analysis [7], modern investigations have yielded a variety of methods for controlling finger growth in a Hele-Shaw cell. The mathematical framework describing viscous fingering was initially developed for a CFR. However, recent control methods, which have introduced time-varying flow parameters, inspire the methods underlying the present investigation. The investigations of [9] produced highly symmetric bubble morphologies by varying the injection pressure to produce a flow rate that decays as a power law with time. The number of symmetric petals formed during injection was controlled by varying a "flux constant." This parameter was later defined for time varying $Q(t)$ by [10] as

$$J(t) = \frac{Q(t)R(t)}{2\pi M_2\sigma} = 3n_m(t)^2 - 1, \tag{5}$$

and used to control viscous fingering subject to restricted flow conditions. Setting flow conditions such that the value of J is time independent, the resulting bubble morphologies are predictable and highly symmetric. The definition in (5) reveals that instability growth is related to a time-varying capillary number based on the characteristic velocity $Q(t)R(t)/2\pi b^2 = R'(t)(R(t)/b)^2$. Further, $J(t)$ is the time-varying analog of the global capillary number [11,12], which is given by $2\pi J(0)$ and defined in terms of the radius, $R(0) > 0$, of an initially unperturbed interface.

A recent, comprehensive study [13] of nonstandard Hele-Shaw setups introduced two geometric parameters (the isoperimetric and circularity ratios) which have the potential to be integrated with experimental data. The investigators used numerical simulations to characterize the stability of Hele-Shaw cell configurations with tapered plates, rotating plates, and time-varying injection rates. Their results suggest that viscous fingering in a Hele-Shaw cell can be suppressed by introducing, either in isolation or together, a tapered gap and time-dependent injection rates.

The effect of an oscillatory flow rate on instability growth has been the subject of previous numerical investigations [1,14]. One investigation found a reduction in fingering extent, which they attributed to a nonlinear finger competition mechanism that leads to bubble detachment at

the interface. For oscillations, 20% of the mean flow rate, the optimal oscillation frequency for instability mitigation by this nonlinear mechanism was reported as $f = 3/t_f$, where t_f is the final time. Another recent investigation [14] found that resonant morphological structures formed (in the nonlinear regime of growth) for certain periods of sinusoidal injection. The authors proposed this phenomenon as a viable method to determine fluid viscosity experimentally.

With the significant progress of these previous efforts to control viscous fingering, we anticipate that investigating time-varying injection schemes will draw further benefits. The power-law flow rate investigated by [9] provides a means to suppress instability growth by wave number and produce symmetric interfacial patterns. However, the control scheme employs a monotonically decreasing flow rate, which could limit some large-scale displacement applications. The investigations of [1] into the stability induced by flow rate oscillations were based on numerical simulations, thus, a logical addition to the collection of recent literature [1,14] regarding injection rate oscillations is an experimental, broader-scale parameter study. As such, the present investigation aims to explore a variety of flow rate oscillations and determine which cases are optimal for stabilizing or destabilizing the interface using a joint experimental and analytical approach. In what follows, the methodology, results, and implications of the experiments, in which air is injected at an oscillatory rate into a radial Hele-Shaw cell filled with a more viscous silicone oil, are outlined. Particularly, in Sec. II, we consider a time-varying flow rate and develop analogous equations to (2)–(5), and conditions for linear stability relative to the CFR case, again neglecting wetting effects. In Sec. III, we present the experimental design we use to inject air at an oscillatory rate into silicone oil in a radial Hele-Shaw cell. We then present and compare the theoretical and experimentally obtained growth in Sec. IV. In Sec. V, we briefly discuss the implications of our stabilizing and destabilizing control schemes, and the limitations of our analysis and experiments. Finally, we summarize our findings and recommendations for future work in Sec. VI.

II. ANALYSIS

Here, we present an analysis based on the results of (2)–(5) modified to account for a time-varying injection rate $Q(t)$. In this case, (2) is rewritten as

$$R(t) = \left(R(0)^2 + \frac{1}{\pi} \int_0^t Q(s) ds \right)^{\frac{1}{2}}. \tag{6}$$

Despite the introduction of a time-dependent flow rate, the radial velocity of the interface retains a simple form

$$R'(t) = \frac{Q(t)}{2\pi R(t)}. \tag{7}$$

Following the analysis in [8] using a variable flow rate yields an analogous linear instability growth rate to that in (3), given by

$$\frac{f_n'(t)}{f_n(t)} = \frac{n-1}{R(t)^2} \left(\frac{Q(t)}{2\pi} - \frac{n(n+1)\sigma M_2}{R(t)} \right), \tag{8}$$

that is consistent with the analysis of [15]. The corresponding wave numbers representing critical and maximal instability growth are similarly modified to account for time-varying flow rates as

$$n_c(t) = \left(\frac{Q(t)R(t)}{2\pi\sigma M_2} + \frac{1}{4} \right)^{\frac{1}{2}} - \frac{1}{2}, \tag{9a}$$

$$n_m(t) = \left[\frac{1}{3} \left(\frac{Q(t)R(t)}{2\pi\sigma M_2} + 1 \right) \right]^{\frac{1}{2}}. \tag{9b}$$

We note that these results also immediately follow from the CFR result (3) since the flow dynamics prescribed by the steady, incompressible form of Darcy's law imply that the only time dependence comes from the kinematic condition at the interface. In particular, we emphasize that we continue to assume that any inertial terms (including those arising from the time-varying flow rate) can be neglected. The analysis performed here also implicitly assumes a separation between the timescale governed by the flow rate $Q(t)$ and the timescale representing the rate of growth of perturbations (i.e., the mean behavior is slow compared to the growth or decay of perturbations). This assumption does not hold where the growth of perturbation amplitude occurs more slowly than the mean flow timescale (such as when we are close to neutral stability), so it is reasonable to expect a reduction in quantitative accuracy of the theoretical predictions in these regimes. However, from an averaging (bracketing) argument, we expect that the analysis should still give useful qualitative predictions in such regimes, albeit with larger quantitative uncertainty.

The linear analysis is valid for times t such that $0 \leqslant t \leqslant t_{\max}$ where nonlinear effects, such as harmonic mixing, tip splitting, and finger competition, become important after $t_{\max}$. A strict criterion for linear stability of the interface relative to its initial condition at $t = 0$ can be derived by analyzing the terms of (8). By considering outward radial flow starting at $t = 0$ and requiring that $f_n'(t) \leqslant 0$, we integrate the corresponding non-negative inequality $R'(t)R(t)^2 \leqslant n(n+1)\sigma M_2$ to determine a bound on $R(t)$, given by

$$R(t) \leqslant \left[R(0)^3 + 3n^*(n^*+1)\sigma M_2 t\right]^{\frac{1}{3}}, \tag{10a}$$

$$Q(t) \leqslant \frac{2\pi n^*(n^*+1)\sigma M_2}{\left[R(0)^3 + 3n^*(n^*+1)\sigma M_2 t\right]^{\frac{1}{3}}}, \tag{10b}$$

where n^* is the smallest (strictly) stable wave number and we have used (6) to determine the $Q(t)$ criterion. The bounds in (10) imply the linear stability of perturbations of wave number $n = n^*, n^*+1, \ldots$ for times $t \in [0, t_{\max}]$. However, strictly requiring $f_n'(t) \leqslant 0$ at all times may not be necessary to produce an effectively stable interface in the linear regime. The solutions $f_n(t)$ to the instability growth function $f_n'(t)$ with $f_n(t_1) = 1$ are defined for a truncated set of wave numbers $n = 1, 2, \ldots, n_{\max}$ as

$$f_n(t) = \left[\frac{R(t)}{R(t_1)}\right]^{n-1} \exp\left[-(n-1)n(n+1)\sigma M_2 \int_{t_1}^{t} R(s)^{-3} ds\right]. \tag{11}$$

The form of the solution expressed in (11) shows that instability growth induced by outward flow is in competition with decay induced by the effects of surface tension. Most of the numerical analysis we employ involves solving (11), subject to the flow rate oscillations analogous to those detailed in Sec. III. However, the underlying techniques are applicable to non-negative, time-varying flow rates that satisfy the steady, incompressible form of Darcy's law.

The reference condition time t_1 is not explicitly defined, and thus can be tailored differently to our theoretical and experimental approaches. In the following analysis [i.e., (12)–(15)], we present simplifications in the instability conditions that arise by specifically defining $t_1 = t_1(n)$ as the smallest time satisfying $n_c(t_1) = n$. This definition implies that a particular mode only begins to grow once it becomes critical. When considering a CFR driven by an area flow rate Q_0, (3) integrates to an analytic solution [16]. We recast this solution in terms of $J_0(t)$ by noting that $J(t_1) = J_0(t_1^0) = n(n+1)$, such that it is expressed as

$$f_n^0(t) = \left[\frac{J_0(t)}{n(n+1)}\right]^{n-1} \exp\left[(n-1)\left(\frac{n(n+1)}{J_0(t)} - 1\right)\right], \tag{12}$$

where subscripts and superscripts of 0 indicate the CFR case, unless otherwise specified. Using the results of (11) and (12), we derive a criterion for stabilization relative to the CFR case when

$R(t) = R_0(t)$, which is given by

$$\frac{\ln\overbrace{\left[\frac{Q(t_1)}{Q_0}\right]}^{\leqslant 1+\xi}+1}{n(n+1)} - \sigma M_2 \int_{t_1}^{t} R(s)^{-3} ds < \frac{1}{J_0(t)}, \tag{13}$$

where we have assumed that the injection rate is constrained by

$$\frac{Q(s)}{Q_0} \geqslant 0 \;\forall\; s \in [t_1, t], \qquad \frac{Q(t_1)}{Q_0} \leqslant 1 + \xi, \tag{14}$$

where $\xi > -1$. The stabilization criterion in (13) is valid for $n > 1$, but this restriction is insignificant since the solution to the linear growth rate equation is trivial for $n = 1$. For the case of outward flow driven by an oscillatory injection rate $\xi < 1$ such that $1 - \xi \leqslant Q(s)/Q_0 \leqslant 1 + \xi \;\forall\; s \in [t_1, t]$. While not exploited in our investigations, the integration-by-parts relationship

$$\sigma M_2 \int_{t_1}^{t} R(s)^{-3} ds = -\frac{1}{2}\left[\frac{1}{J(t)} - \frac{1}{n(n+1)} + 4\pi^2 \sigma M_2 \int_{t_1}^{t} \frac{R''(s)}{Q(s)^2} ds\right] \tag{15}$$

may garner further insight into the relationship between the acceleration of the interface, capillary effects, and linear instability growth assuming the steady form of Darcy's law. For example, consider the optimal injection scheme derived by [17] via a Euler-Lagrange equation, which assumes that $J(t) \gg 1$. With fixed initial and final conditions, the optimality condition is given by $R'' = 0$, thus producing a linearly increasing flow rate and simplifying the stabilization term. We emphasize that the solution does not incorporate wetting and viscous stress effects, for which analogous growth rate expressions have been developed for a CFR [18]. In Appendix A, we include these effects in the CFR growth rate equation to derive a modified equation governing n_m and an instability growth solution including wetting (but not viscous stress) effects.

III. EXPERIMENTAL METHODS

The analytical predictions developed in Sec. II are experimentally tested using a radial Hele-Shaw cell apparatus outlined here. Two 19-mm-thick glass plates (381 mm × 381 mm), flat to less than 1 λ at 633 nm, with a uniform spacing enforced at each corner using shim supports ($b = 1 \pm 0.05$ mm) are supported in a tub filled with silicone oil (ClearCo 50 cSt silicone fluid: density $\rho_2 = 960$ kg/m^3, viscosity $\mu_2 = 0.048$ Pa s, surface tension $\sigma = 0.022$ N/m) so that the free surface lies at the bottom of the top plate and leveled to within 0.2° such that gravity acts uniformly on the cell (Fig. 2). Air is injected through a centrally drilled hole on the top plate. An analog, peristaltic pump (Masterflex L/S Economy Drive, Model 77200-60), operating at 5 Hz provides a nominally constant mean flow rate (see Appendix B for a characterization of the peristaltic flow rate), while the superimposed oscillations are produced by a zero mean flow rate oscillatory pump (Fluid Metering Inc, STQP Adjustable High Flow Stepper Pump) with a custom frequency control board (Fluid Metering Inc, SCST-01), providing a constant stroke volume V_h. For the oscillations, three different frequency regimes are considered based on increasing (nominal) pulse frequency f_{pn}: LF (low frequency, $f_{pn} = 0.17$ Hz), IF (intermediate frequency, $f_{pn} = 2.7$ Hz), and HF (high frequency, $f_{pn} = 10.7$ Hz). Platinum-cured silicone tubing (Masterflex L/S Precision Pump Tubing, Model 96410-16) is used for all connections. A square area (20.4 cm × 20.4 cm) in the free surface plane, containing the air-silicone interface, is imaged at 60 Hz using a SA4 Photron camera with a 1024 pixel × 1024 pixel CMOS sensor, fitted with a 50-mm macro lens and a resulting resolution of 5 pixels/mm.

The resulting air-silicone oil interface is represented by the area it encloses, $A(t) = \frac{\pi}{n_{\text{int}}} \sum_{m=1}^{n_{\text{int}}} r(\theta(m), t)^2$, where r is the distance of each interface point from the center of the frame (and origin of the coordinate system). The average interfacial radius is taken as $R(t) = (A(t)/\pi)^{1/2}$.

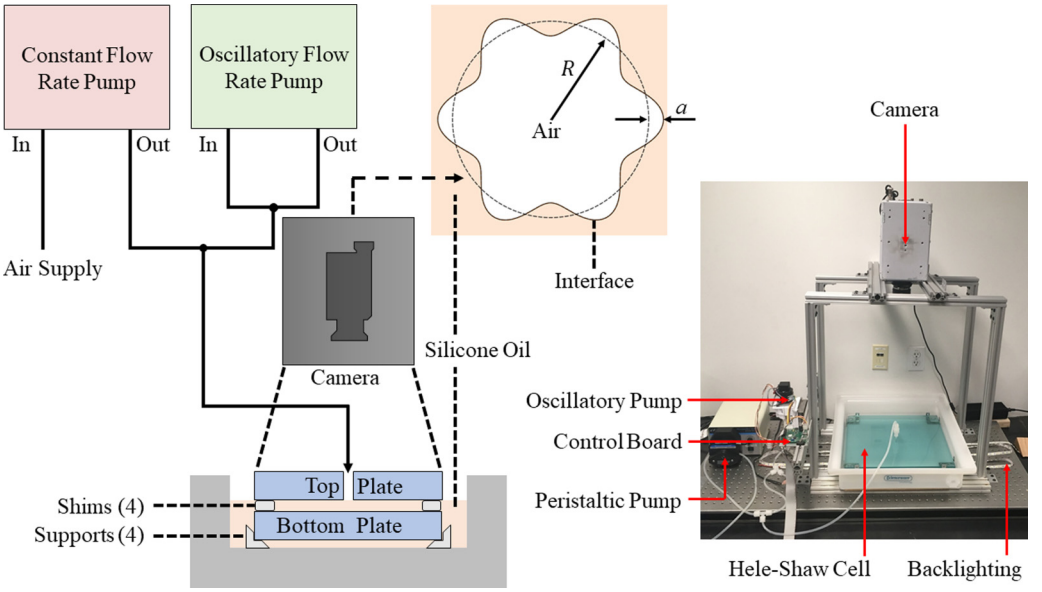


FIG. 2. Experimental apparatus: air is pumped into a radial Hele-Shaw cell with silicone oil as the working fluid. The air-silicone oil interface growth is imaged with a high-speed camera.

The interface contour is detected on each of the acquired images and subsequently discretized. Image preprocessing includes background subtraction, contrast enhancement, and Gaussian filtering. A Sobel edge is used for interface detection. Prior to discretization, the interface is dilated to allow for missing point replacements and subsequently eroded to one pixel, thus accurate to the originally detected outline within a pixel. To maintain roughly consistent spacing between points as the radius grows, the number of discretization points $n_{\rm int}$ increases according to $n_{\rm int} = n_0(1 + \frac{b^2}{R(0)^2}\frac{t}{t^*})^{1/2}$, where $t^* = \frac{\pi b^2}{Q_0}$, while $R(0)$ and n_0 are the average interfacial radius (see Appendix B) and number of discretization points at $t = 0$, respectively. Finally, postprocessing of the discretized interface includes filtering (and linear interpolation to maintain uniforming spacing) when noise higher than five median absolute deviations from the median radius is present. The parameter $n_0(= 50)$ is chosen such that spatial resolution is balanced with noise amplification when computing geometrical parameters at small radii.

The reference timescale $t^*(= 1.91$ ms) equating the area enclosed by the interface to that enclosed by a circle with a radius of one gap width b is taken as constant and computed using the mean Q_0 produced by the CFR experiments (discussed below). This timescale is derived from a purely geometric basis, and was previously employed in [19]. The oscillatory parameters ξ and f_p are not considered in formulating t^* to simplify the geometric comparisons of instability growth in the following sections. More generally, the timescale $t_g^* = \pi R(t)^2/Q(t)$ is associated with the first term of (8) and relevant on the oscillation timescales, but we do not use it for normalization since it varies in time. Instead, we discuss its relevance to the experimental results in Sec. V. Alternate timescales can be derived by considering each term in the growth rate equation (3) for the CFR case and taking $R_0(0) = 0$. Neglecting wave-number dependencies, the terms scale as $(2t)^{-1}$ and $(t^3/\tau^{**})^{-1/2}$, respectively, where $\tau^{**} = \pi^3\sigma^2 M_2^2/Q_0^3$.

Regarding the time interval considered $t \in [0, t_{\rm max}]$, where $t = 0$ is the first frame where an interface contour can be identified and $t_{\rm max}(= 5230t^*)$ is chosen as the limit after which nonlinear growth becomes prominent and affects the interface detection: the choice is based on visual inspection (see also Fig. 7 and Supplemental Material [20]), field of view constraints, and discretization

TABLE I. The pulse frequencies ($\bar{f}_p t^*$), stop-band frequencies ($f_{\text{stop}} t^*$), and time interval $[\tau_1, \tau_2]$ used to fit the flow rates of each experimentally investigated case. Here, $\bar{f}_p$ is the mean frequency estimate (as in Appendix B). For the LF and IF cases, f_{stop} is taken as the peristaltic pump frequency; however, for the HF case, f_{stop} is increased since $\bar{f}_p t^* > 9.55 \times 10^{-3}$.

Case	$\bar{f}_p t^*$	$f_{\text{stop}} t^*$	τ_1/t^*	τ_2/t^*
LF	3.11×10^{-4}	9.55×10^{-3}	0	$t_{\max}$
IF	5.15×10^{-3}	9.55×10^{-3}	524	$\tau_1/t^* + 10(f_{\text{pn}} t^{*-1})$
HF	2.06×10^{-2}	2.75×10^{-2}	524	$\tau_1/t^* + 10(f_{\text{pn}} t^{*-1})$

requirements (the interface radius is single valued for every angular coordinate, i.e., the interface contour does not fold onto itself). The cutoff time associated with accurate interfacial detection is slightly earlier in our HF.b case (described in Table II, Appendix B), and as such we reduce the maximum time for the plots in Fig. 4 to $t_{\max} = 4700 t^*$.

Once the interface contour has been discretized, $A(t)$ is used to determine the representative flow rate parameters. Specifically, in the case of the CFR experiments, where the interface area grows almost linearly over time, the mean flow rate Q_0 is estimated as the slope of a least-squares fit of $A(t)$. For the oscillatory cases, a least-squares finite impulse response (FIR) differentiation filter (50th order) is applied to $A(t)$ to create an experimental $Q(t)$ signal. The pass-band and stop-band frequencies are denoted as f_{pass} and $f_{\text{stop}} = 1.2 f_{\text{pass}}$, respectively. A nonlinear least-squares fit of $Q(t)$ is then used to estimate the oscillatory flow rate parameters: Q_0, $\xi = Q_h/Q_0$, f_p, and t_0 (assuming a sinusoidal harmonic oscillation of magnitude $Q_h = 2\pi f_p V_h/b$ superimposed on a mean flow rate Q_0, with a time phase shift t_0). The validity of this assumption is discussed in Appendix B (Fig. 8). The phase shift t_0 is attributed to slight variations in the startup process of the oscillatory pump and in the minimum detectable interface in each run. A note should also be made regarding the time interval $[\tau_1, \tau_2]$ used for the nonlinear fit in the oscillatory cases (see Table I). For the LF case $\tau_1 = 0$ and $\tau_2 = t_{\max}$, covering approximately two cycles. For the IF and HF cases, the first 60 frames ($\tau_1/t^* = 524$) are omitted to remove any influence of the peristaltic pump's startup (which can be significant on the timescales $(f_p t^*)^{-1}$), and τ_2 is chosen such that the interval covers ten full cycles while eliminating early onset of nonlinear growth that could contaminate the parameter fit (see, e.g., Fig. 7). The resulting mean pulse frequencies $\bar{f}_p$ are within 1% (IF, HF) and 2% (LF) of their nominal values f_{pn}, supporting the above assumptions on the flow behavior and thresholds used. All the estimated parameters for both oscillatory and nonoscillatory (CFR) experiments, together with appropriate estimation errors, can be found in Appendix B.

Based on our theoretical and experimental methods, a stability analysis follows in the next section. To quantify global interfacial instability, we adopt the geometric parameters defined in [13]. The isoperimetric ratio $I(t)$ is an indicator of the overall deformation (i.e., stretching) of the interface from its most stable (circular) configuration. The circularity ratio $C(t)$ quantifies the maximum extent of the deviations from a circular interface. These ratios are defined as

$$I(t) = \frac{L(t)^2}{4\pi A(t)}, \quad C(t) = \frac{\max\{r(\theta, t)\}}{\min\{r(\theta, t)\}}, \tag{16}$$

where $L(t)$ is the interface perimeter. Both ratios consider a two-dimensional interface (as in Fig. 2) and are normalized such that the minimum value is unity for a circular interface. Isolated spikes in the records of $I(t)$ and $C(t)$ that remain are removed from $I(t)$ and $C(t)$, and the resulting gap is filled by linear interpolation, if they lie more than three median absolute deviations away from the local moving median over 25 frames ($= 220 t^*$). We also decompose the perturbations of the interface about the mean radius using the discrete Fourier transform. As the interface expands, its stability is characterized by the development of perturbations of different wave numbers.

IV. RESULTS

A. Theoretical predictions

The selections for the parameters of oscillation $R(0)$, f_p, and ξ (for fixed Q_0) influence both the value of $n_{\max}$ over a fixed time interval and the growth of instabilities over $n = 1, 2, \ldots, n_{\max}$. Two types of oscillations starting at $t = 0$, those with $\xi > 0$ and those with $\xi < 0$, are considered from a numerical standpoint. Consistent with (12)–(15), here an instability of wave number n is only predicted to grow once it becomes critical, as defined by (9a). Hence, an initial instability amplitude is defined as $f_n(t_n) = 1$ at the earliest time $t_1(n)$ at which each wave number becomes critical. Employing this constraint and neglecting wave-number-dependent variations in A_n, as defined in (1), allows for consistent growth comparisons for different wave numbers. Numerical simulations may eliminate this simplification by determining the actual distribution of A_n, which is likely sensitive to experimental conditions. Using these definitions, $n_{\max}$ is set as the maximum value of $n_c(t)$ over $t \in [t_1(n), t_f]$. For a truly CFR case (but not necessarily the oscillatory cases), $n_{\max} = n_c(t_f)$ since $Q(t) = Q_0$ never decreases.

One measure of the stabilization of the interface relative to the CFR case during injection over a time interval is the ratio of instability growth at the end of the interval. Under the present assumptions, this parameter is given by

$$\epsilon = \frac{f_n(t_f)}{f_n^0(t_f)}, \tag{17}$$

where t_f is the (final) time, and $f_n(t_f)$ and $f_n^0(t_f)$ are the predicted instability growth values at this time for flow driven by $Q(t)$ and Q_0, respectively. The frequencies considered numerically are chosen as the relevant mean frequencies (over five experiments) for the optimal LF ($\bar{f}_p t^* = 3.24 \times 10^{-4}$), IF ($\bar{f}_p t^* = 5.15 \times 10^{-3}$), and HF ($\bar{f}_p t^* = 2.05 \times 10^{-2}$) oscillation experiments shown in Sec. IV B. In each of these cases, the variation in ϵ over $n = 1, 2, \ldots, n_{\max}$ and $\xi \in [-1, 1]$, as predicted by (11), is shown in Fig. 3. To ensure that Q_0 is the mean flow rate over the interval (within a relative error of 0.5%) and $R(t_f)/R_0(t_f) = 1$ (within 0.16%) for the frequencies selected for experiments, the final time is set to $t_f/t^* = (3.24 \times 10^{-4})^{-1}$.

The range of unstable wave numbers differs significantly for LF oscillations of magnitude ξ depending on whether the oscillation amplitude increases ($\xi > 0$) or decreases ($\xi < 0$) initially, as seen in Fig. 3. While the stabilized wave numbers tend to be near $n_{\max}$ for $\xi > 0$, they occupy significant ranges below $n = 15$ for small oscillations and below $n = 10$ for large oscillations when $\xi < 0$. At higher frequencies, the most attenuated wave numbers at a given ξ are centered around $n_{\max}$ as computed for the CFR case, and their spread in n increases with both $|\xi|$ and f_p. Further, as seen in Fig. 9 in Appendix C, somewhat similar qualitative behavior is obtained when considering (for all cases) an additional (sinusoidal) peristaltic waveform with amplitude of 48.6% the mean CFR. The depicted variations in ϵ essentially reflect the degree to which the condition in (13) is (not) met, with the equality case separating stable and unstable wave numbers. If we instead replaced $Q(t_1)/Q_0$ with $1 + |\xi|$, ϵ would be overpredicted, and thus the stable regions in (ξ, n) would be smaller.

Step increases in $n_{\max}$ occur when $|\xi|$ is increased sufficiently such that a perturbation of a larger integer wave number is predicted to grow when $n_c(t) = n_{\max}$. The times associated with these jumps are determined by the behavior of $J(t)$. As f_p increases, (de)stabilization relative to the CFR case converges in both locations in (ξ, n) space and in magnitude of instability attenuation (amplification). While our predictions are based on idealized theory that neglects wetting, nonlinear, and unsteady effects and assume perturbation growth starts once a mode becomes critical, we test their compatibility with analogous experiments in the following section. We only consider experiments with positive oscillations since the consideration of negative oscillations would require additional modifications to ensure that a sufficiently developed mean flow is available for the oscillatory pump to draw from during startup at the beginning of the interval.

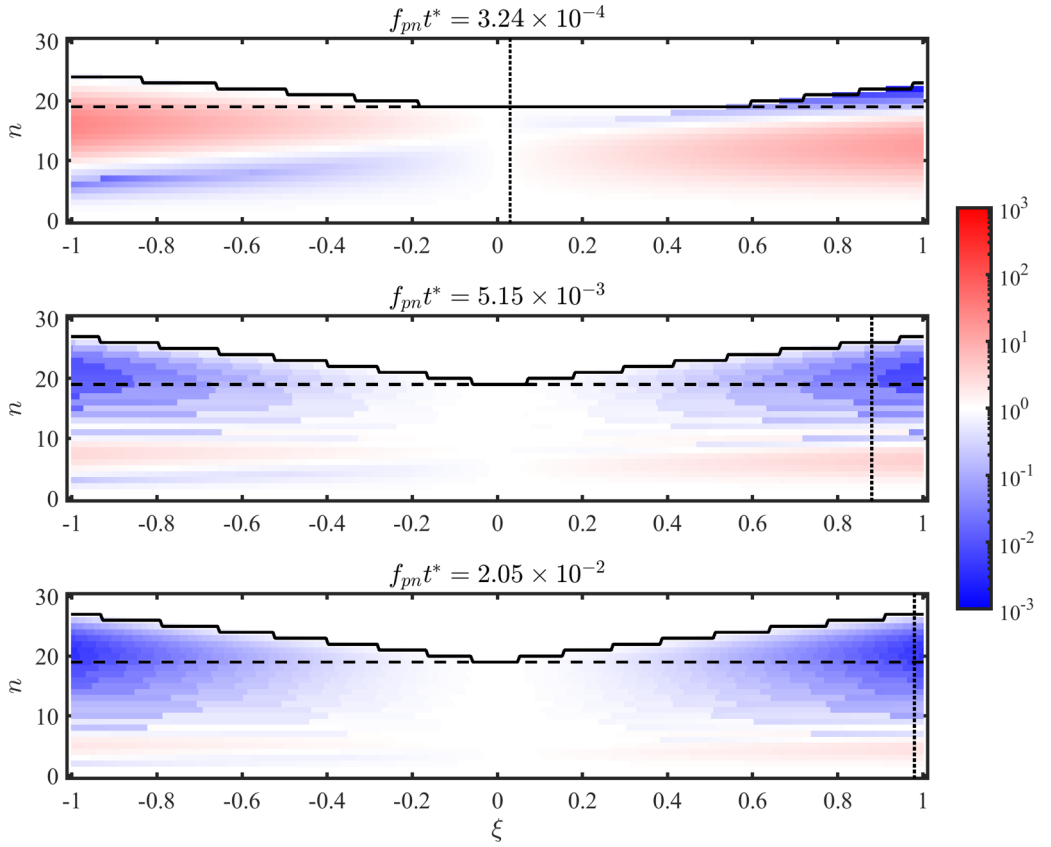


FIG. 3. Log-scale color mapping of ϵ over the range of pertinent wave numbers and all values of ξ for strictly outward flow driven by $Q(t)$, with $\xi < 0$ (left) and $\xi > 0$ (right) oscillations starting at $t = 0$. Since ϵ is a measure of instability relative to flow driven by the CFR Q_0, blue (red) coloring corresponds to regions of relative stability (instability) of the interface produced by $Q(t)$. For each (ξ, n), the maximum value of $n_c(t)$ over $t \in [t_1(n), t_f]$ is plotted for the oscillatory flow rate (solid) and CFR (dashed) case. The vertical dotted lines correspond to the optimal experimental parameter combinations detailed in Sec. IV B. Identical plots to these that incorporate additional peristaltic variations into the instability predictions are shown in Fig. 9 in Appendix C.

B. Experimental results

The development of the isoperimetric and circularity ratios provides insight into the influence of the combined growth of (and relative phases between) all modes on the interfacial morphology during bubble expansion. Larger values of $I(t)$ and $C(t)$ are indicative of a more unstable interface. A comparison of the development of both ratios during injection for different oscillation frequencies and the corresponding amplitudes ξ is shown in Fig. 4. Provided ξ is positive for the experiments conducted, the interface strictly expands in the radial direction for $\xi < 1$, whereas it periodically grows and shrinks for $\xi > 1$. For all cases, similar trends in interfacial stability are observed for the isoperimetric and circularity ratios.

The stability of the air-oil interface is tracked for all oscillations considered in Figs. 4(a) and 4(b). Comparisons of the optimally stabilizing cases ($\bar{f}_p t^* = 3.24 \times 10^{-4}$ and $\bar{f}_p t^* = 2.05 \times 10^{-2}$) and the optimally destabilizing case ($\bar{f}_p t^* = 5.15 \times 10^{-3}$) are shown in Figs. 4(c) and 4(d). Overall instability growth relative to the CFR case is reduced (increased) when one or both of the $I(t)$ and $C(t)$ curves track below (above) the plane (or curve) representing the CFR case. The LF, low-magnitude ($\xi = 0.03$) oscillations result in a reduction in instability with regards to both ratios

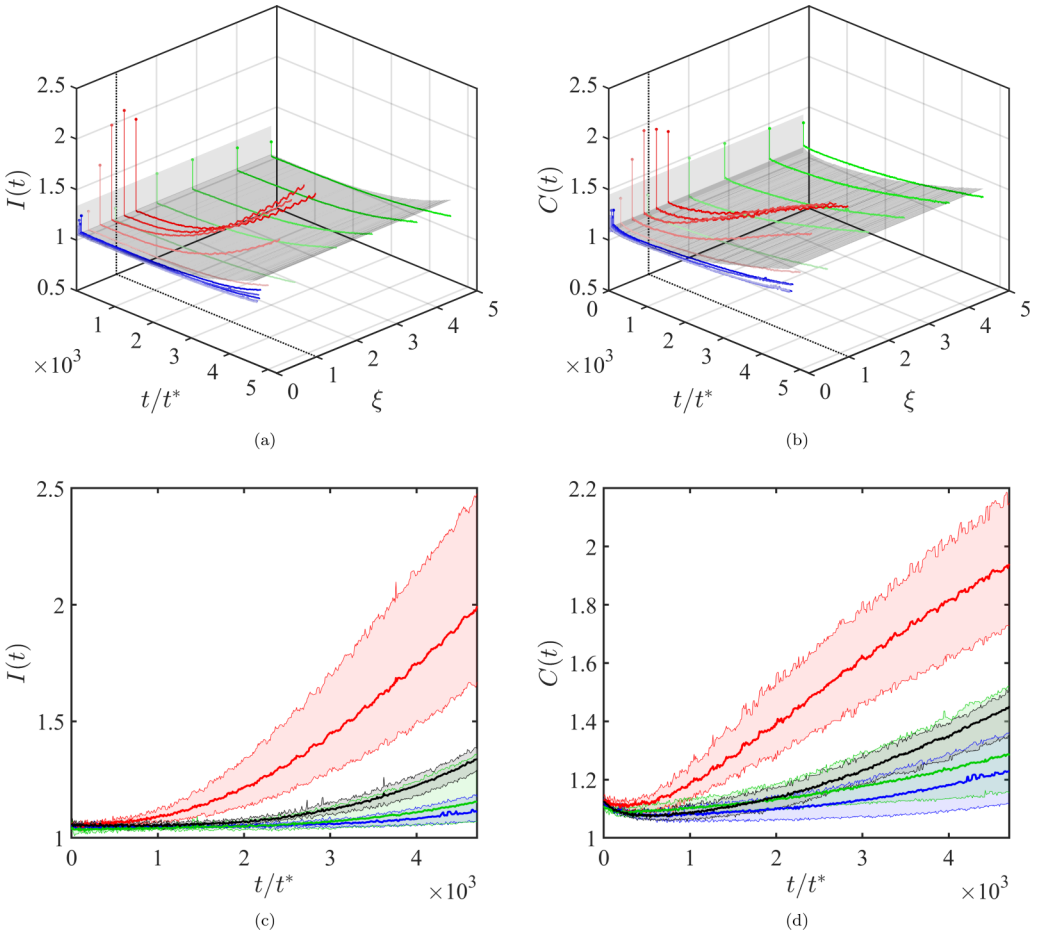


FIG. 4. The time evolution of the mean isoperimetric (a) and circularity (b) ratios for each set of five experiments: LF (blue), IF (red), and HF (green) oscillations are compared to those produced by the CFR (gray surface). The shading of each line in (a) and (b) corresponds to the stroke volume for a given frequency setting (darker for larger stroke volumes). The magnitude of oscillation scales with its frequency because the oscillatory pump operates with a constant stroke volume. The range of values (vertical line) and maximum value (circle) for each curve are projected onto the plane at $t = 0$. The means (thick lines) and ranges (shaded regions) of the isoperimetric (c) and circularity (d) ratios are plotted for the most stabilizing LF and HF oscillations, the most destabilizing IF oscillations, and the CFR case (black line, gray shading). The optimal IF experiments are more unstable than the CFR experiments in the linear regime, whereas the optimal LF experiments are more stable than the CFR experiments. While the optimal HF oscillations stabilize the interface on average, they do not outperform the LF oscillations and have large variation across the five experiments.

during the interval. A similar effect is seen to a lesser extent when HF oscillations with larger flow rate oscillations ($\xi = 0.98$) are present. The most unstable cases occur in the IF experiments, which most significantly destabilize the interface when $\xi = 0.88$.

While the isoperimetric and circularity ratios are informative measures of instability, they do not provide a complete view into the mechanisms by which flow rate oscillations stabilize or destabilize the interface. We next consider individual Fourier modes of $a(\theta, t)$ in θ for positive integer wave numbers. In the linear regime, the magnitudes of the perturbations are small and the growth of each mode is assumed to be independent of all other modes. The magnitude of each mode can be normalized by $R(t)$ to represent the growth of instabilities relative to the growth of the

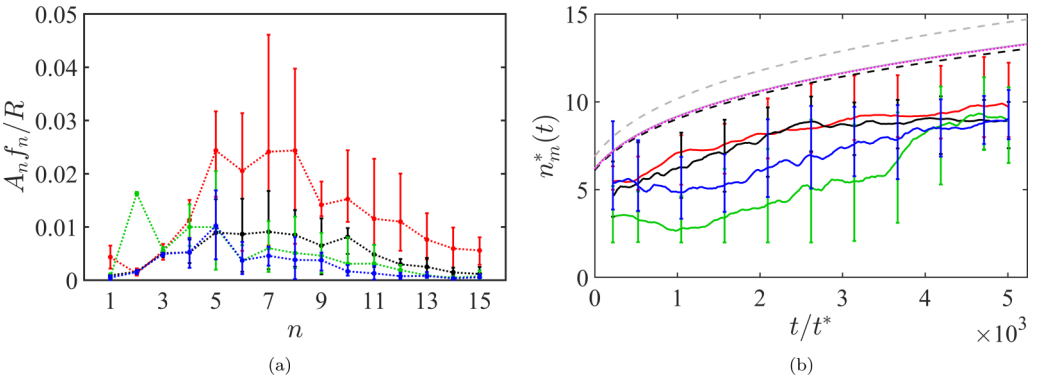


FIG. 5. Characteristics of perturbation growth by wave number based on the data collected over five repeated experiments using LF (blue), IF (red), and HF (green) oscillations and the CFR only (black). (a) The growth of each mode relative to the mean interfacial radius $A_n f_n(t)/R(t)$ of the first 15 Fourier modes n of the zero-mean wavelike perturbation of the interface at $R(t)/b = 55$. (b) Moving averages (window size: $524t^*$) of the mean (solid lines) and range (error bars at end points and selected interior points with 1 s spacing) of the maximally growing wave number at each time step. For each experiment, 25 frames ($= 220t^*$) from each end of the time series are removed upon differentiation of the growth data. The smooth curves represent the theoretical n_m for a CFR $Q_0 = 16.45\,\mathrm{cm}^2/\mathrm{s}$ using Eqs. (4b) (black dashed), (A4) with $(\gamma, \delta) = (0, 0)$ (gray dashed), (A4) with $(\gamma, \delta) = (\frac{2}{3}, 0)$ (gray solid), and (A4) with $(\gamma, \delta) = (\frac{2}{3}, 1)$ (magenta dotted). Note that the difference between black dashed and gray dashed lines is attributable to the static capillary factor.

mean interfacial radius. Here, instead of neglecting the spatial parameter A_n, as in the analysis of Sec. IV A, it is now built into our spatial representation of each mode, given by $A_n f_n$.

The average relative growth of each mode when the mean interfacial radius is $R(t)/b = 55$ is compared for the optimally stabilizing and destabilizing cases and the CFR case in Fig. 5(a). While the IF oscillations reliably increase the mean growth of nearly all wave numbers, the LF and HF oscillations selectively mitigate the growth of larger wave numbers ($n > 5$) in the linear regime. Here, the most unstable wave numbers in the CFR case range from $n = 5$ to 10. As compared to the CFR case, the HF oscillations result in increased growth of wave numbers $n < 5$. Further, there is significant variation in the growth of each mode across five trials for nearly all wave numbers.

In an experimental setting, $n_m^*(t)$ is more easily estimated from experimental data than the $n_c^*(t)$ since $A_n f_n$ is typically smaller than both the experimental resolution and the error tolerances when n is critical, and $n_m > n_c$ for outward flow. By differentiating the growth of each wave number (using a 50th-order FIR differentiator) the experimental growth rate of each wave number is determined. Moving averages of the experimental estimates of the (integer) maximally growing wave numbers (n_m^*) for the optimal cases are shown in Fig. 5(b). The stabilizing oscillations (LF and HF) are associated with reductions in the typical n_m^* relative to the CFR case, whereas n_m^* is marginally larger in the destabilizing (IF) case. However, for all cases, n_m^* is smaller than that predicted by the linear theory for a CFR. A similar discrepancy was also observed in the estimated n_c in experiments subject to pressure oscillations [21]. Similarly, the CFR experiments of [8] found that the wave number of perturbations is typically n_m at inception, but decreases as the instability develops.

To capture the behavior of n_m^*, we reconsider the surface tension σ, which relates the pressure drop across the interface to curvature related to the growth of wavelike perturbations through the Young-Laplace equation. The analysis of [21] accounted for variations in the pressure drop across the interface by introducing an effective surface tension σ^* as a function of the critical wave number estimated from experiments. We modify this approach by expressing the effective surface tension as a function of the (time varying) $n_m^*(t)$:

$$\frac{\sigma^*(t)}{\sigma} = \frac{J(t)}{3n_m^*(t)^2 - 1}. \tag{18}$$

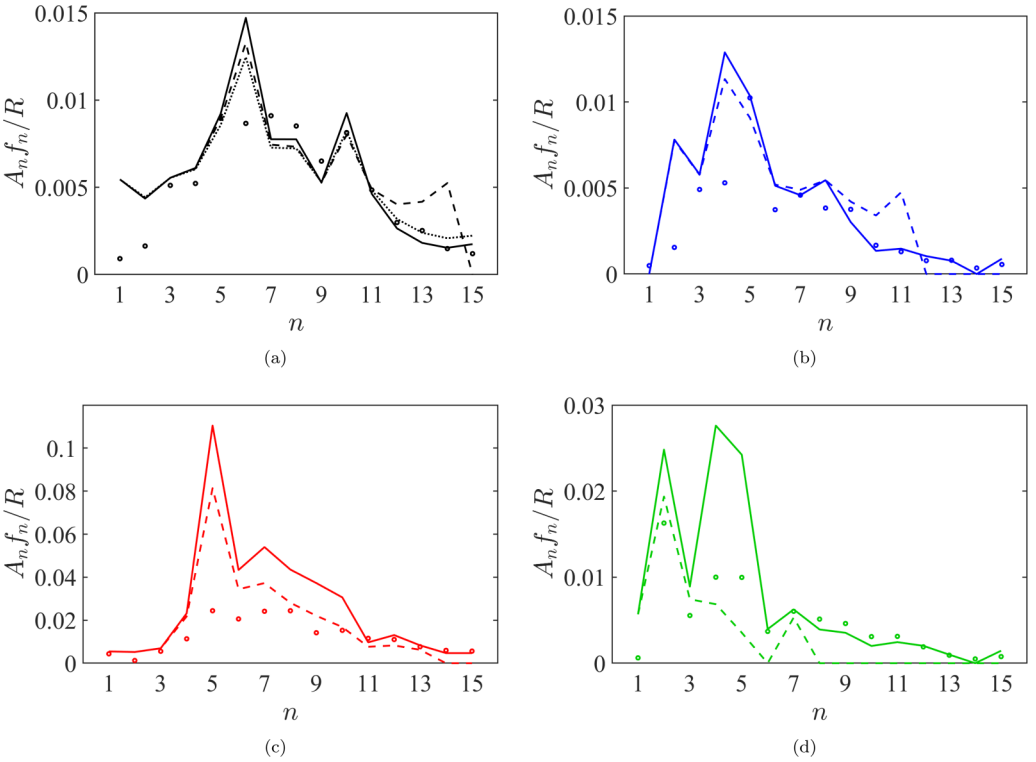


FIG. 6. Predictions (standard: solid line, modified with $\sigma^*(t)$: dashed line) and mean experimental values (open circles) of the relative growth $A_n f_n(t)/R(t)$ of each wave number when $R(t)/b = 55$ are shown for the CFR case (a) and the optimal LF (b), IF (c), and HF (d) cases. We define a reference time t_1 as in (11) such that $A_n f_n(t_1)/b = 0.3$, and $f_n(t)$ goes to zero if this threshold is not met, or if the solutions are predicted to decay until $t = t_1$. In (a), the dotted black line corresponds to the solution (A6) with $(\gamma, \delta) = (\frac{2}{3}, 0)$, i.e., including the effects of wetting.

The accuracy of the linear predictions of (18) is improved by setting t_1 such that $A_n f_n(t_1)/b = 0.3$ to distinguish the excitation of a particular mode from experimental noise, which is typically below this threshold. However, with this modified definition, each mode is no longer critical at t_1. Therefore, these experimental reference times differ in nature from those considered theoretically (see Secs. II and IV A).

A prediction similar to that in (11) can be made by incorporating information about $n_m^*(t)$ by replacing σ with $\sigma^*(t)$. In effect, this modification introduces a (maximally growing) wave-number dependence into a linear growth equation, thus relaxing the assumption that the growth of perturbations of each wave number is independent. Since $A_n f_n(t_1)/b = 0.3$ is fixed, (11) can be used to directly predict instability growth when $R(t)/b = 55$. Comparisons of the standard linear prediction, the modified prediction incorporating $\sigma^*(t)$, and the experimentally estimated growth at $R(t)/b = 55$ are shown for each case in Figs. 6(a)–6(d). These predictions are relatively accurate for the CFR and LF ($\bar{f}_p t^* = 3.24 \times 10^{-4}$) oscillation cases. For the IF ($\bar{f}_p t^* = 5.15 \times 10^{-3}$) and, to a lesser extent, the HF ($\bar{f}_p t^* = 2.05 \times 10^{-2}$) oscillations tend to overpredict the growth of the most unstable wave numbers. Similar results can be produced by replacing $\sigma^*(t)$ with its mean over the whole interval shown in Fig. 5(b), but would not reflect the observed variations in $n_m^*(t)$ for HF (and IF) oscillations. Introducing σ^* can account for the unmodeled static capillary factor of $\pi/4$ in the second term of (11) and the influence of, e.g., wetting or viscous stresses on the observed n_m^*. For example, neglecting viscous stresses ($\delta = 0$) in the CFR case, it can be expected that $\frac{\sigma^*}{\sigma} > \frac{\pi}{4}$ since

dynamic wetting effects act to reduce n_m in the linear regime when the $\pi/4$ factor excluded in (8) is included [22], as shown in Fig. 5(b). However, the form of the instability growth equation corrected for wetting and viscous stress effects [see (A1) in Appendix A] reveals that σ^* alone cannot fully capture the influence of these physical effects, which modulate other terms as well. In future work, these predictions may be useful in theoretically or numerically determining the optimal type of oscillations for a given application using some initial instability information.

In addition to quantitative comparisons, we present a qualitative comparison of the interfacial morphology at $R(t)/b = 55$ for representative trials of the optimally stabilizing and destabilizing cases and the CFR case in Fig. 7. The depicted interfaces indicate that the stabilizing and destabilizing trends observed in the isoperimetric ratio, circularity ratio, and relative growth of each wave number are qualitatively realized during experiments.

V. DISCUSSION

The numerical results shown in Sec. IV A provide a mapping of the (de)stabilization of the interface driven by $Q(t)$ relative to one driven by Q_0 alone, based on the predictions of (11). While experimentally untested in this investigation, the numerically predicted properties of negative oscillations are promising, in that stabilization is centered around lower wave numbers which become critical early during the injection interval. This scheme is also desirable in considering that, consistent with the results of other studies [21,22], the experimental data suggest that the maximally growing wave number is lower than that predicted by the linear theory (neglecting wetting) in most experiments. Further, this $Q(t)$ has qualitative similarities to the optimal injection scheme derived by [17], in which the flow rate varies linearly with time during injection. The corresponding assumption that $J(t) \gg 1$ is valid for our CFR case (i.e., $J_0 \gg 1$), but not necessarily for oscillations with large amplitude.

Experimentally, we consider the stabilizing and destabilizing effects of three distinct regimes of injection rate oscillations. The first regime is characterized by LF oscillations of small amplitude ($\xi < 1$). These oscillations require the lowest power input into the stepper motor driving the oscillatory pump, yet produce the most stabilized interface of all oscillations considered. Nevertheless, considering the low magnitude of the LF.a oscillations (Table II, Appendix B), we emphasize this case also reflects adding a second, zero-mean flow rate pumping system, which may have an uncharacterized effect on the stability. A low-power-input stabilizing mechanism can be used to prolong the linear stability of the interface without significantly modifying the mean interfacial displacement. Similarly, the large HF injection rate fluctuations may serve as an alternative mechanism for interfacial stabilization, as the instability growth profiles (e.g., at $n = 2$) and the $I(t)$ and $C(t)$ traces are markedly different than the LF cases.

The IF oscillations of magnitudes close to the mean flow rate ($\xi \sim 1$) most effectively destabilize the interface as compared to the CFR case by exciting a broad range of unstable wave numbers. The increases in $I(t)$, $C(t)$, and $A_n f_n/R$ for this case are the most drastic changes observed relative to the CFR case out of all cases tested. The ability to amplify the growth of the instabilities may improve the efficiency of mixing at low Reynolds numbers (e.g., in a microfluidic channel, see [4]).

Since the number of frames sampled per oscillation decreases as the oscillation frequency increases, the uncertainty of the nonlinear least-squares flow rate fit increases with frequency, as seen in Appendix B. This effect can be amplified for HF oscillations by the peristaltic variations of the nominally constant mean flow rate, which act on similar timescales to $(f_p t^*)^{-1}$.

Consistent with other studies that neglect wetting effects [8,16], we omit the static capillary prefactor of $\pi/4$ on the in-plane curvature term of the Young-Laplace equation based on the matched asymptotics of [23] (and included by, e.g., [11,12,22]). The dynamic wetting term, also derived in [23], scales as $Ca_l^{2/3}$, where

$$Ca_l(t) = \frac{\mu_2}{\sigma}\frac{Q(t)}{2\pi R(t)} \tag{19}$$

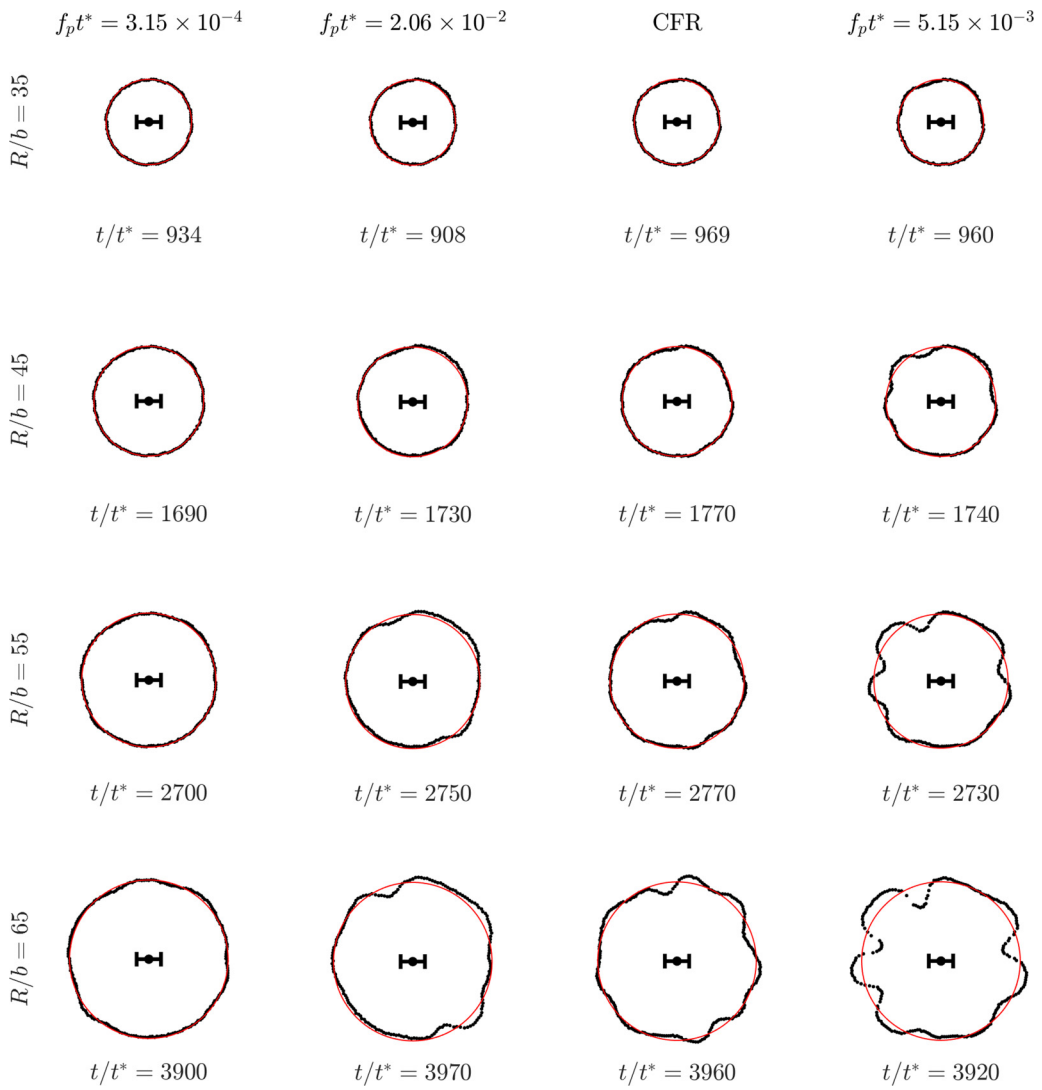


FIG. 7. Comparisons at increasing radii of the interfaces from typical experiments with the optimal oscillatory flow rates and the CFR. The mean radii (red) shown are computed from the uniformly spaced boundaries (black) representing the interfaces. The experiments with LF [far left, $R(0)/b = 15.5$] and HF [middle left, $R(0)/b = 17.5$] oscillations visually mitigate the growth of instabilities at the interface as compared to the CFR case [middle right, $R(0)/b = 14.6$]. The IF oscillations [far right, $R(0)/b = 14.7$] amplify the growth of perturbations at the interface. The times shown give a rough comparison of the mean flow rates for the four experiments across each row, but neglect the differences in the flow rates prior to the interfaces reaching $R(0)$ for each experiment. The scale bars are 2 cm (or 20 gap widths) long segments centered at the point of injection (black dot).

is the local capillary number. As noted by [22], for the CFR case the static and dynamic wetting effects act to stabilize the interface and reduce the maximally growing wave number, but do not shift the range of unstable wave numbers. This behavior is consistent with the fact that the dynamic wetting correction factor $(2/b)C_0 Ca_l^{2/3}$ (where $C_0 \approx 3.80$ [23]) remains above 10% of the out-of-plane term (i.e., $2/b$) in the Young-Laplace equation when $Ca_l \approx 0.00427$, which

corresponds to $R_0(t)/b \approx 134$ for the CFR case. The unstable behavior for the IF case may be influenced by dynamic wetting effects in the vicinity of the interface. As seen in the Supplemental Material [20], the optimal IF case sustains visual variations in the film wetting thickness longer than the other cases. This behavior is consistent with the fact that the IF oscillations ($\xi \sim 1$) and their timescale $1/\bar{f}_p = 0.371$ s are of similar magnitudes, respectively, to the mean CFR and its (time-varying) timescale $t^*_{g,0} = \pi R_0(t)^2/Q_0$, particularly when $R_0(t)/b \sim 13.9$. Another potentially relevant "characteristic" timescale, $t_{ch,0} = \frac{t^*_{g,0}(0)}{2\pi J_0(0)}$, is defined in terms of the CFR and an initially unperturbed radius, and its time-varying analog can be expressed as $t_{ch} = \frac{t^*_g(t)}{2\pi J(t)}$. The timescale $t_{ch,0}$ is related to a resonant flow oscillation period $T_{res}(M_1/M_2, t_{ch,0})$, that has been shown to amplify instability growth, causing fingers to emerge earlier [14]. However, the present investigation considers a mobility ratio $M_1/M_2 \sim O(10^3)$, whereas [14] considered $M_1/M_2 \sim O(10^2)$. We do not speculate further into these amplified mechanisms observed in the IF cases since they are beyond the scope of our investigations. While the steady form of Darcy's law, which we employ, has been widely used to model steady flows in porous media, an unsteady form is often employed to capture unsteady effects. In oscillatory channel flow, the timescale associated with the unsteady term decreases to $\frac{5}{6}$ of its LF limit value in the HF limit since the viscous layer depth decreases (i.e., the wall-normal velocity profile becomes more uniform) at sufficiently high frequencies [24]. The unsteady timescale ρM is related to the angular oscillation frequency $\omega = 2\pi f_p$ through the Womersley number $\alpha = \sqrt{3\rho M \omega}$. For the present experiments, $\rho M \approx 5.64$ ms (air) and 1.67 ms (silicone oil) produces $\alpha \lesssim 1$ for both fluids and all frequencies considered. It would be interesting to investigate instability growth for flow governed by the unsteady form of Darcy's law, where the choice of timescale is particularly important. Additionally, the significant variations in the excitation of different modes across experiments imply that a receptivity-like investigation of the development of local excitations resulting from experimental inhomogeneities would improve predictive capabilities for time-varying injection processes. These variations appear to increase in magnitude as the oscillation frequency increases, holding V_h constant. This increase is attributed to large, rapid variations in $n_c(t)$ and $n_m(t)$.

Tailoring injection rate oscillations to either amplify or attenuate the growth of relevant modes in the experimental regime (determined, in part, by the mean flow rate) is a versatile method for influencing instability growth. While the growth of different wave numbers relative to each other during experiments can be reasonably captured by the theoretical predictions for IF and HF oscillations, there is notable discrepancy in the case of LF oscillations. This difference is driven, in part, by the difference between the predicted and observed maximally growing wave numbers during the injection period. One possible explanation is that wetting effects, which are more significant at smaller radii, damp the instability more significantly during the positive stroke of the LF oscillation. The variations in $n^*_m(t)$ are accounted for by utilizing the notion of an effective surface tension, modified from [21] to consider $n^*_m(t)$, since it is more easily tracked than $n^*_c(t)$ in an experimental setting and contains information of the most unstable wave numbers. Further, our definition is consistent with the fact that wetting effects reduce the predicted $n^*_m(t) < n_m(t)$, but are not predicted to modify $n^*_c(t)$ in the linear regime for the CFR case [22]. Moving forward, predictions of instability growth by wave number in a radial Hele-Shaw cell, as in (11), are likely to be improved by accurately modeling the dynamics, i.e., by including wetting, nonlinear, and possibly unsteady effects, governing the emergence and growth of perturbations.

VI. CONCLUSION

The growth of the Saffman-Taylor instability in a radial Hele-Shaw cell, subject to an oscillatory injection rate with nonzero mean, is investigated in both numerical and experimental contexts. From a numerical standpoint, predictions of the growth of wavelike perturbations of relevant wave numbers are made using the linear growth formulation neglecting wetting effects, as derived in

Sec. II. It is shown that, for $n < n_{\max}$, LF oscillations with $\xi > 0$ ($\xi < 0$) are predicted to be more unstable (stable) for smaller wave numbers and more stable (unstable) for larger wave numbers. However, as the frequency is increased, the predicted effects of both $\xi > 0$ and $\xi < 0$ oscillations converge to similar results for $|\xi| < 1$. Similar trends were observed for modified analyses taking into account a simple representation of the peristaltic fluctuations of the base flow introduced in the experiment.

Three regimes of injection rate oscillations produced by a constant stroke volume oscillatory pump are considered. Control schemes for mitigating the Saffman-Taylor instability typically rely on monotonically decreasing the injection rate [9,10] or introducing large variations from the mean flow rate [13]. By contrast, the schemes we present are desirable since they preserve a constant phase-averaged flow rate and require minimal flow rate modulation. The LF, low-magnitude ($\xi = 0.03$) oscillations most consistently stabilize the interface to the largest extent (on average) out of all oscillations considered, but may also reflect the influence of the peristaltic oscillations in the experimental pumping mechanism. The stability induced by this oscillatory scheme would improve the yield and effectiveness of displacement processes in applications, such as secondary oil recovery, which aim to minimize the growth of fingers. It would be worthwhile to see whether the peristaltic variations influence the observed stability, i.e., if similar stabilization can be achieved with a truly constant mean injection rate.

The optimally destabilizing IF oscillations ($\xi = 0.88$) reliably and significantly amplify the growth of the most unstable wave numbers in the linear regime and result in a more rapid transition to nonlinear growth. These effects are beneficial in applications such as microfluidic mixing due to the increased interfacial surface area. In addition, our Supplemental Material [20] suggests that dynamic wetting variations near the interface may persist throughout the nominally linear regime for the destabilizing IF cases.

In contrast to the IF oscillations, the optimal HF oscillations ($\xi = 0.98$) have a stabilizing effect on the interface; however, due to the early amplification of low wave numbers, this stabilizing effect is weaker than that of the LF oscillations. The most significant (de)stabilization is seen for $n > 5$ when subject to (IF) LF and HF injection rate oscillations. Similar to the LF case, the peristaltic pump is an experimental limitation in the HF case since its nominal frequency is slower than the HF oscillations. Employing digitally controlled pumps to produce the CFR may help more accurately address the influence of injection rate oscillations, particularly in the LF and HF cases considered.

The observed stabilizations for LF (and HF) oscillations with $\xi > 0$ are associated with reductions in n_m^* as compared to the CFR case. Consequently, the stabilizing effect cannot be predicted by linear theory alone; however, as shown in Sec. IV B, the accuracy of the predictions can be improved by incorporating minimal experimental data to set the reference condition associated with (11) at a point where the large influences of early wetting (and startup) effects are at least partially captured. Notably, consistent with the results of [22] for a CFR, the experimental growth of $n_m^*(t)$ is generally overpredicted by the linear theory without the wetting correction factor or consideration of the experimental peristaltic base flow fluctuations for nearly all flow rates considered.

While the present experiments are limited to the consideration of oscillations with $\xi > 0$, the linear predictions for $\xi < 0$ show considerable mitigation of the wave numbers ($n < 15$) observed to dominate the experimental regimes considered. These predictions warrant future investigations considering LF oscillations with $\xi < 0$ since they show the potential to more effectively mitigate instability growth compared to the $\xi > 0$ case, and do so in a manner better predicted by linear theory.

The instability growth solution (11) becomes truly analytic in cases where the imposed control law produces $R(t)$ such that $R(t)^{-3}$ is integrable and t_1 is known. Relatively permissible ranges of flow rate parameters can be determined by the conditions in (10) based on the range(s) of wave numbers predicted to be most unstable. Since this study only considers the linear growth of perturbations of the interface, investigations of interfacial stability in the nonlinear regime of finger growth would be beneficial for applications which require large flow rates (and consequently

enter the nonlinear regime earlier). For time-varying flow rates, we also anticipate that further characterizing the wetting and unsteady effects associated with flow rate oscillations will help elucidate mechanisms underlying the (in)stability of the interface. Depending on the flow regime, potentially important considerations include capturing all timescales relevant to the flow as well as global and local capillary effects.

More broadly, the radial Hele-Shaw cell is desirable in a laboratory setting since the interface is continuously defined with no in-plane solid boundaries and the plates provide a homogeneous setting during displacement. As such, an analogous study considering the effect of flow rate oscillations in a linear Hele-Shaw cell, where the boundary conditions at the interface must be accounted for, would be beneficial. Further, one notable difference between Hele-Shaw cells and porous media is the irregularity associated with the latter. Therefore, investigating finger growth subject to flow rate oscillations in an inhomogeneous porous medium would help determine the feasibility of the present oscillatory schemes in practical settings.

ACKNOWLEDGMENTS

The support of Student Faculty Programs at California Institute of Technology for the Summer Undergraduate Research Fellowship Program and, in particular, that of B. and L. Alpinieri, is gratefully acknowledged. We are grateful for M. Li's contribution to an earlier experiment related to the Hele-Shaw problem.

APPENDIX A: WETTING AND VISCOUS STRESS EFFECTS FOR A CONSTANT FLOW RATE

The generalized linear growth rate accounting for wetting effects and viscous normal stresses for the CFR case [18] is given by

$$\frac{1}{f}\frac{df}{dt} = \frac{1}{1+s_n(t)+w_n(t)}\left[\frac{(n-1)}{R(t)^2}\left(\frac{Q}{2\pi} - \frac{\pi}{4}\frac{n(n+1)\sigma M_2}{R(t)}\right) + \frac{Qs_n(t)}{2\pi R(t)^2}\left(\frac{n+3}{n+1}\right)\right], \tag{A1}$$

where, consistent with other studies that consider wetting effects [11,12,22,23], we retain the static capillary factor $\pi/4$. The wetting term is

$$w_n(t) = n\frac{G_0}{R(t)^\gamma} = \gamma n\frac{C_0}{6}\frac{b}{R(t)}Ca_l(t)^{\gamma-1}, \quad G_0 = \gamma C_0\frac{b}{6}\left[\frac{2\pi}{Q}\frac{\sigma}{\mu_2}\right]^{1-\gamma}, \tag{A2}$$

where $Ca_l(t)$ is the local capillary number, $C_0 = 3.80$, and $\gamma = \frac{2}{3}$ (or 0) when wetting effects are (not) considered. The viscous normal stress term is

$$s_n(t) = \delta\frac{n(n+1)}{6}\left[\frac{b}{R(t)}\right]^2 = 2\delta\frac{n(n+1)M_2\mu_2}{R(t)^2} = G_1\frac{n(n+1)}{R(t)^2}, \tag{A3}$$

where $G_1 = 2\delta k_D$, $k_D = b^2/12$ is the Darcian permeability, and $\delta = 1$ (or 0) when viscous stress effects are (not) considered.

The maximally growing wave number is given by the solution to the following quartic (cubic, quadratic) polynomial for the case where $\delta = 1$ and $\gamma = \frac{2}{3}$ ($\delta = 0$ and $\gamma = \frac{2}{3}$, $\delta = 0$ and $\gamma = 0$):

$$\begin{aligned} &R(t)^{3+\gamma}\left[2QR(t) - \pi^2\sigma M_2(3n^2-1)\right] + 2R(t)^3\left[QR(t) - \pi^2\sigma M_2 n^3\right]G_0 \\ &- R(t)^{1+\gamma}\left(2QR(t)[n(n-4)-4] + \pi^2\sigma M_2\left(n^2+n\right)^2\right)G_1 \\ &- 4n^2QR(t)^\gamma G_1^2 + 2QR(t)^2n^2G_1G_0 = 0. \end{aligned} \tag{A4}$$

Assuming that the mode becomes critical when $t = t_1(n)$ and retaining the $\pi/4$ factor in (A1), the radius at the critical time is

$$R(t_1) = \frac{\pi}{4}\frac{2\pi}{Q}M_2\sigma n(n+1). \tag{A5}$$

In cases where viscous stresses can be neglected ($\delta = 0$), (A1) can be integrated to obtain a solution for linear instability growth including wetting effects for a CFR. By noting the definitions of $w_n(t)$ and $R(t_1)$ in (A2) and (A5), respectively, we express this solution as

$$f_n(t) = \left[\frac{R(t)}{R(t_1)}\left(\frac{1+w_n(t)}{1+w_n(t_1)}\right)^{\frac{1}{\gamma}}\right]^{n-1} \exp\left[\left(\frac{n-1}{1-\gamma}\right)\left(\frac{R(t_1)}{R(t)}\frac{{}_2F_1\left(1,1-\frac{1}{\gamma},2-\frac{1}{\gamma},-\frac{1}{w_n(t)}\right)}{w_n(t)}\right.\right.$$
$$\left.\left. - \frac{{}_2F_1\left(1,1-\frac{1}{\gamma},2-\frac{1}{\gamma},-\frac{1}{w_n(t_1)}\right)}{w_n(t_1)}\right)\right], \tag{A6}$$

where ${}_2F_1$ is the Gauss hypergeometric function.

APPENDIX B: FLOW RATE ESTIMATES AND ERRORS

For each injection rate considered, the parameters of oscillation and mean flow rates, as defined in Sec. III, are shown in Table II. Outliers more than three standard deviations from the original fit are excluded in the final fit. Only the mean flow rate Q_0 is estimated for the constant flow rate (CFR) experiments. The value of $\hat{\sigma}$ represents the standard deviation of the estimated parameter over five trials. The value of $\hat{\sigma}_p = [\frac{1}{N_{tot}-5}\sum_{k=1}^{5}(N_k-1)s_k^2]^{1/2}$ represents the pooled standard deviation of each parameter estimate, where s_k and N_k are the standard error of the parameter estimate and the number of frames used for the kth experiment, such that $N_{tot} = \sum_{j=1}^{5} N_j$. Since we consider the same group size for identical experiments, the assumption of homogeneity of variance is justified. The delayed startup of the oscillatory pump corresponds to a negative value of $\hat{\mu}$ for t_0. This delay is resolved only for the low-frequency (LF) cases since, for the intermediate- (IF) and high- (HF) frequency cases, $1/f_p$ is on a similar scale to t_0 and we exclude the first 60 frames. Thus, for

TABLE II. The estimated flow rate parameters ($\hat{\mu}$) and error estimates ($\hat{\sigma}$ and $\hat{\sigma}_p$) over five trials of each experimental setting are rounded to two decimals (for Q_0 and all values less than 1) and three digits (otherwise). Low- (LF), intermediate- (IF), and high- (HF) frequency oscillation schemes are imposed using five different volume stroke settings, each denoted by a letter a–e.

Parameter	Q_0 (cm^2/s)			$f_p t^*(10^{-4})$			ξ			t_0/t^*		
Value	$\hat{\mu}$	$\hat{\sigma}$	$\hat{\sigma}_p$	$\hat{\mu}$	$\hat{\sigma}$	$\hat{\sigma}_p$	$\hat{\mu}$	$\hat{\sigma}$	$\hat{\sigma}_p$	$\hat{\mu}$	$\hat{\sigma}$	$\hat{\sigma}_p$
CFR	16.45	0.04	0.01									
LF.a	16.52	0.02	0.04	3.24	0.10	0.14	0.03	0	0	−185	25.0	125
LF.b	16.48	0.02	0.04	3.03	0.07	0.08	0.05	0	0	−234	26.3	68.5
LF.c	16.41	0.10	0.04	3.09	0.06	0.06	0.07	0	0	−288	21.2	48.3
LF.d	16.27	0.02	0.04	3.08	0.03	0.04	0.09	0	0	−335	36.0	31.7
LF.e	16.18	0.03	0.04	3.15	0.02	0.03	0.12	0	0	−313	33.5	25.2
IF.a	16.48	0.04	0.05	51.5	0.04	0.04	0.3	0.01	0	36.1	31.5	1.45
IF.b	16.60	0.08	0.05	51.6	0.08	0.02	0.59	0.01	0.01	22.3	19.3	0.78
IF.c	16.58	0.02	0.06	51.5	0.04	0.02	0.88	0.01	0.01	10.9	24.5	0.55
IF.d	16.73	0.07	0.05	51.5	0.01	0.01	1.19	0.03	0.01	22.4	18.2	0.36
IF.e	16.69	0.17	0.06	51.5	0.02	0.01	1.49	0.02	0.01	74.9	104	0.37
HF.a	16.27	0.26	0.95	205	1.12	0.95	0.98	0.05	0.10	−11.6	16.0	4.50
HF.b	16.32	0.28	0.93	206	0.66	0.45	2.01	0.05	0.14	−10.2	15.5	2.13
HF.c	16.68	0.27	0.96	206	0.53	0.31	2.9	0.13	0.19	−18.5	15.0	1.47
HF.d	16.64	0.28	0.97	206	0.29	0.22	4.02	0.18	0.25	−30.6	2.74	1.03
HF.e	16.75	0.36	0.99	206	0.22	0.19	4.86	0.29	0.3	−18.5	17.9	0.90

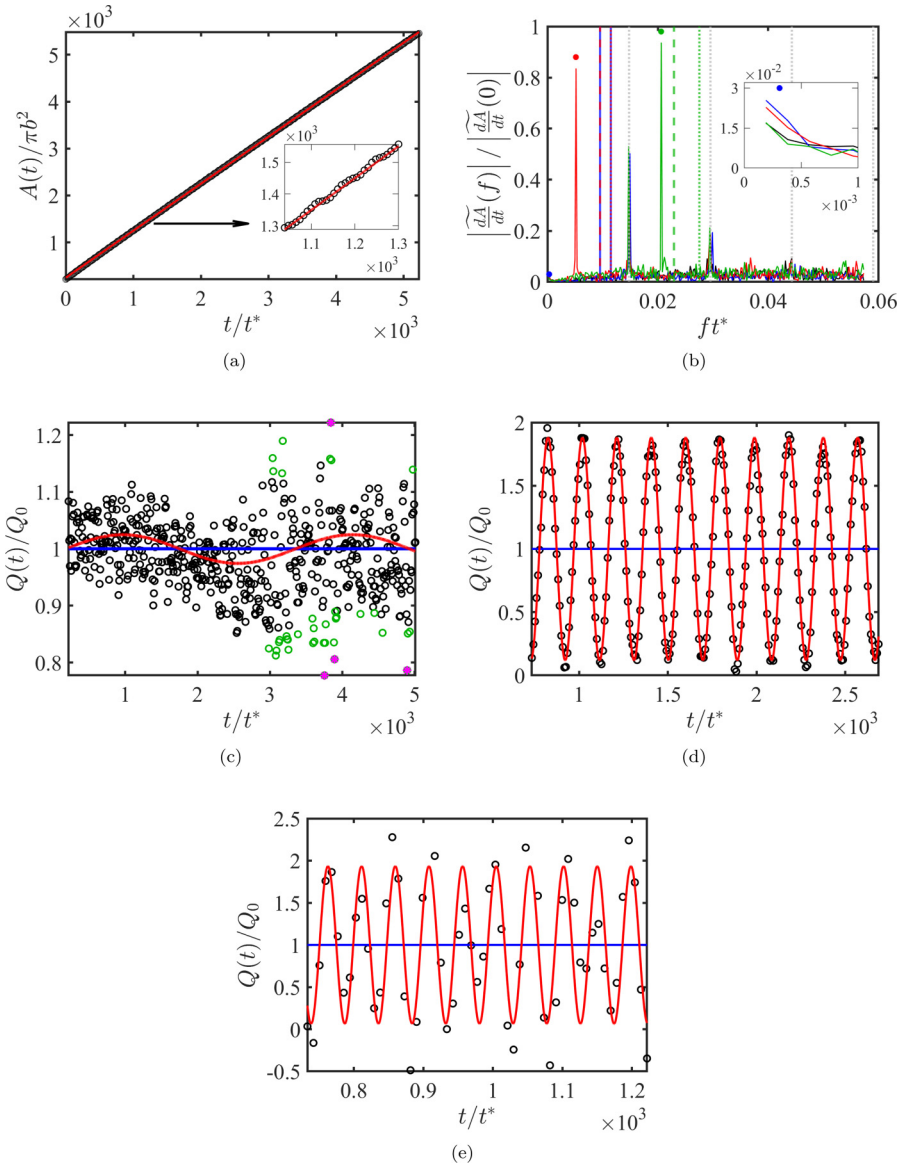


FIG. 8. (a) The image-processed time evolution (black circles) and linear fit (red) of the area enclosed by the interface for the CFR case shown in Fig. 7 and (inset) a closeup of the peristaltic variations over 30 frames [i.e., 3.86 nominal peristaltic oscillation periods; here, the peristaltic pump nominally operates at the frequency of its largest harmonic at ($f_{\text{per}}t^* = 0.0148$)]. (b) Fourier spectrum (inset: closeup in the LF regime) of the time differences $\frac{dA}{dt} = \frac{\Delta A}{\Delta t}$ of the experiments shown in Fig. 7, where 3 padding zeros have been added (to the 600 frame signal) for the HF.a case. The large dots represent the mean frequencies reported in Table II for the LF.a, IF.c, and HF.a experiments (respectively) and the corresponding dashed (dotted) vertical lines represent the pass-band and stop-band frequencies. The peristaltic harmonics (dotted gray lines) decrease with increasing frequency, so although variations at the fourth (i.e., highest-frequency) harmonic are not resolved, they are expected to be of small magnitude. The area injection rate oscillations about the mean (blue) for the optimal (b) LF, (c) IF, and (d) HF cases, as in Fig. 7, where, in (b), outliers (magenta stars) more than three standard deviations away from a fit of all 550 points are excluded from the final fit (red). For the LF case, the black (green) circles are less (more) than two standard deviations from the final fit, and no points meet this threshold for the IF and HF cases shown.

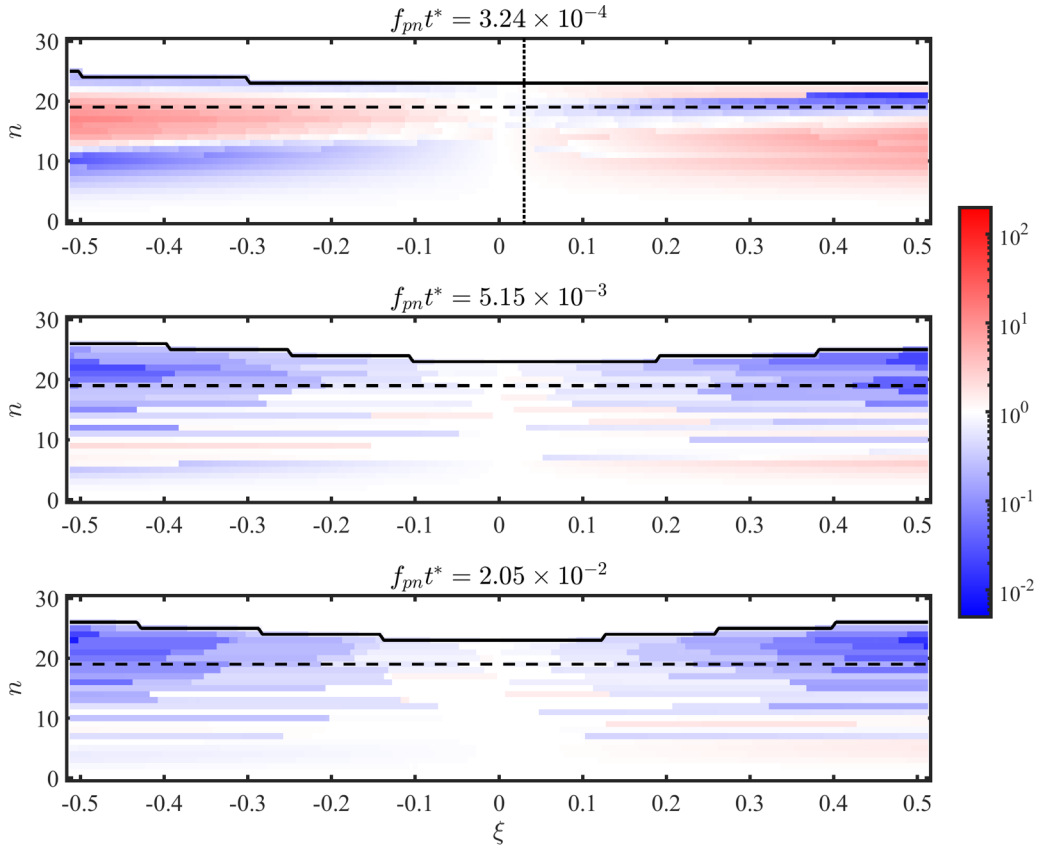


FIG. 9. The same plots as Fig. 3, but shown for a sinusoidal flow rate with an additional sinusoidal peristaltic waveform $Q_p \sin(2\pi f_{\text{per}} t)$ added about the mean flow rate for all cases considered. A constant $Q_p = 0.486 Q_0$ based on the magnitude of the first peristaltic harmonic is set for the CFR case in Fig. 8(b). Using this value, the oscillatory parameter is limited to $\xi \leqslant 0.51$ to maintain a positive injection rate. The ξ-axis and color (ϵ-axis) limits in this plot differ from those in Fig. 3.

the IF and HF cases, we report the equivalent value of t_0 with the smallest magnitude. The mean interfacial radius in the first frame, averaged ($\pm$ one standard deviation) over all 80 experiments, is $R(0)/b = 16.2 \pm 1.4$.

Figures 8(a)–8(e) show, respectively, the linear fit of the area enclosed by the interface $A(t)$ for the CFR case, the Fourier spectra of the optimal experiments, and the nonlinear least-squares fits of $Q(t)$ for the optimal LF, IF, and HF cases, as depicted in Fig. 7. The inset plot shows one limitation of our experiments, the peristaltic nature of the mean flow rate supplied by the nominally CFR pump. The effects of the peristaltic fluctuations can be seen for the HF case in Fig. 8(e) in the noticeable peak amplitude variations. These variations occur since (i) there are only approximately six points per HF oscillation and (ii) these HF oscillations occur on smaller timescales than the peristaltic variations, which we do not filter to preserve the HF waveform. Nevertheless, as seen in Fig. 8(d), the 10 IF oscillations are consistent and well fit. In Fig. 8(c), the noise level is attributed mostly to the scale of the imposed oscillations and the fact that not all noise from the peristaltic variations can be filtered out during differentiation. For this LF case the initial fit (not shown) using all 550 points is visually nearly identical to the final fit (shown). Collectively, the results of Fig. 8 support the assumption of an approximately constant phase-averaged mean injection rate.

APPENDIX C: LINEAR INSTABILITY GROWTH INCLUDING A PERISTALTIC WAVEFORM

The instability predictions in Fig. 3 consider a truly CFR as the reference case, which gives the corresponding growth $f_n^0(t_f)$, as in (17). As shown in Fig. 8(b), the first harmonic of the peristaltic fluctuations is non-negligible (roughly half the mean injection rate) and correspondingly they have an influence on the instability growth when included in the model (11). In Fig. 9, we incorporate the peristaltic variations into all cases (including the CFR) and find qualitatively similar overall features to those in Fig. 3, but with noticeable modulation in the scale and distribution of stable in unstable regions in (ξ, n) space.

[1] M. Nicotra, Radial fingering in a Hele-Shaw cell, Master's thesis, Politecnico di Milano, Milan, Italy, 2012, https://www.politesi.polimi.it/handle/10589/47722

[2] L. Surguchev, A. Koundin, O. Melberg, T. Rolfsvag, and W. P. Menard, Cyclic water injection: improved oil recovery at zero cost, Pet. Geosci. **8**, 89 (2002).

[3] I. Brailovsky, A. Babchin, M. Frankel, and G. Sivashinsky, Fingering instability in water-oil displacement, Transp. Porous Media **63**, 363 (2006).

[4] B. Jha, L. Cueto-Felgueroso, and R. Juanes, Synergetic Fluid Mixing from Viscous Fingering and Alternating Injection, Phys. Rev. Lett. **111**, 144501 (2013).

[5] A. A. Osiptsov, S. A. Boronin, E. M. Zilonova, and J. Desroches, Managed Saffman-Taylor instability during overflush in hydraulic fracturing, J. Pet. Sci. Eng. **162**, 513 (2018).

[6] S. Berg and H. Ott, Stability of CO_2-brine immiscible displacement, Int. J. Greenhouse Gas Control **11**, 188 (2012).

[7] P. G. Saffman and G. I. Taylor, The penetration of a fluid into a porous medium or Hele-Shaw cell containing a more viscous liquid, Proc. R. Soc. London A **245**, 312 (1958).

[8] L. Paterson, Radial fingering in a Hele Shaw cell, J. Fluid Mech. **113**, 513 (1981).

[9] S. Li, J. S. Lowengrub, J. Fontana, and P. Palffy-Muhoray, Control of Viscous Fingering Patterns in a Radial Hele-Shaw Cell, Phys. Rev. Lett. **102**, 174501 (2009).

[10] Z. Zheng, H. Kim, and H. A. Stone, Controlling Viscous Fingering Using Time-Dependent Strategies, Phys. Rev. Lett. **115**, 174501 (2015).

[11] S. J. Jackson, D. Stevens, D. Giddings, and H. Power, Dynamic-wetting effects in finite-mobility-ratio Hele-Shaw flow, Phys. Rev. E **92**, 023021 (2015).

[12] S. J. Jackson, H. Power, D. Giddings, and D. Stevens, The stability of immiscible viscous fingering in Hele-Shaw cells with spatially varying permeability, Comput. Methods Appl. Mech. Eng. **320**, 606 (2017).

[13] L. C. Morrow, T. J. Moroney, and S. W. McCue, Numerical investigation of controlling interfacial instabilities in non-standard Hele-Shaw configurations, J. Fluid Mech. **877**, 1063 (2019).

[14] T. F. Lins and J. Azaiez, Resonance-like dynamics in radial cyclic injection flows of immiscible fluids in homogeneous porous media, J. Fluid Mech. **819**, 713 (2017).

[15] E. O. Dias and J. A. Miranda, Control of radial fingering patterns: A weakly nonlinear approach, Phys. Rev. E **81**, 016312 (2010).

[16] J. A. Miranda and M. Widom, Radial fingering in a Hele-Shaw cell: a weakly nonlinear analysis, Phys. D (Amsterdam) **120**, 315 (1998).

[17] E. O. Dias, E. Alvarez-Lacalle, M. S. Carvalho, and J. A. Miranda, Minimization of Viscous Fluid Fingering: A Variational Scheme for Optimal Flow Rates, Phys. Rev. Lett. **109**, 144502 (2012).

[18] E. O. Dias and J. A. Miranda, Wavelength selection in Hele-Shaw flows: A maximum-amplitude criterion, Phys. Rev. E **88**, 013016 (2013).

[19] J. D. Chen, Growth of radial viscous fingers in a Hele-Shaw cell, J. Fluid Mech. **201**, 223 (1989).

[20] See Supplemental Material at http://link.aps.org/supplemental/10.1103/PhysRevFluids.5.123902 for movies showing examples of the time evolution of the experimental interfaces for the CFR, LF, IF, and HF cases.

[21] N. Gland and D. Pisarenko, Pressure oscillation effects on the Saffman-Taylor instability, in *Thermo-Hydro-Mechanical Coupling in Fractured Rock*, edited by H.-J. Kümpel (Birkhäuser, Basel, 2003), pp. 977–988.

[22] P. H. A. Anjos and J. A. Miranda, Radial viscous fingering: Wetting film effects on pattern-forming mechanisms, Phys. Rev. E **88**, 053003 (2013).

[23] C. W. Park and G. M. Homsy, Two-phase displacement in Hele Shaw cells: theory, J. Fluid Mech. **139**, 291 (1984).

[24] T. Zhu and M. Manhart, Oscillatory Darcy flow in porous media, Transp. Porous Media **111**, 521 (2016).